Published in final edited form as:
IEEE Trans Biomed Eng. 2010 October ; 57(10): 2335–2345. doi:10.1109/TBME.2010.2051227.

Modelling the Role of the Coronary Vasculature During External Field Stimulation

Martin J. Bishop,
Computing Laboratory, University of Oxford, Oxford OX1 3QD, UK

Patrick M. Boyle [Student Member IEEE],
Department of Electrical and Computational Engineering, University of Calgary, Calgary, AB, Canada

Gernot Plank,
Institute of Biophysics, Medical University of Graz, Graz, Austria and Oxford e-Research Centre, University of Oxford, Oxford, UK

Donald G. Welsh, and
Smooth Muscle Research Group and the Department of Physiology and Biophysics, University of Calgary, Calgary, AB, Canada

Edward J. Vigmond [Member IEEE]
Department of Electrical and Computational Engineering, University of Calgary, Calgary, AB, Canada

Abstract

The exact mechanisms by which defibrillation shocks excite cardiac tissue far from both the electrodes and heart surfaces require elucidation. Bidomain theory explains this phenomena through the existence of intramural virtual electrodes (VEs), caused by discontinuities in myocardial tissue structure. In this study, we assess the modelling components essential in constructing a finite element cardiac tissue model including blood vessels from high resolution MR data and investigate the specific role played by coronary vasculature in VE formation, which currently remains largely unknown. We use a novel method for assigning histologically-based fibre architecture around intramural structures and include an experimentally-derived vessel lumen wall conductance within the model. Shock-tissue interaction in the presence of vessels was assessed through comparison with a simplified model lacking intramural structures. Results indicate that VEs form around blood vessels for shocks > 8 V/cm. The magnitude of induced polarisations is attenuated by realistic representation of fibre negotiation around vessel cavities, as well as the insulating effects of the vessel lumen wall. Furthermore, VEs formed around large sub-epicardial vessels reduce epicardial polarisation levels. In conclusion, we have found that coronary vasculature acts as an important substrate for VE formation, which may help interpretation of optical mapping data.

Keywords

Defibrillation; Bidomain model; Blood vessels

martin.bishop@comlab.ox.ac.uk.

Europe PMC Funders Author Manuscripts

I. Introduction

DEFIBRILLATION by the timely-application of a strong electric shock remains the only reliable means of terminating lethal cardiac arrhythmias. However, our understanding of how externally applied electric fields interact with cardiac tissue structure to successfully activate a sufficient mass of myocardium (> 80 – 90% [1], [2]), especially tissue distant from external surfaces, remains incomplete.

Theoretical considerations based on bidomain theory provide an explanation for experimental observations of oppositely polarised shock-induced regions throughout the myocardium distant from physical electrodes, as if caused by “virtual electrodes” (VEs). It has been postulated that such far-field VE polarisations (VEP) in the tissue bulk arise due to heterogeneity in either applied electric field or tissue structure [3]. Since heterogeneity in the applied field quickly attenuates in the far-field, the primary mechanism for bulk VEP is thought to be structural heterogeneity in the tissue either arising from syncytial heterogeneities [4] (providing the necessary condition of unequal anisotropy ratios is met [3]) or resistive discontinuities. Essentially, for shock-induced intracellular current to traverse a resistive discontinuity, current must exit the intracellular domain on one side (passing into the extracellular domain) and reenter it on the other, depolarising one side of the structure, and hyperpolarising the other [5]. Resistive discontinuties are found in the intracellular space at various spatial scales including gap junctions [6], blood vessels, intersistial clefts [7], fatty/connective tissue deposits and fibre branching/anastomosis. Syncytial heterogeneities [4] inlclude fibre rotation and curvature [8].

Direct experimental evidence of intramural VEs remains inconclusive. Optical measurements are limited since they cannot directly relate changes in recorded transmembrane voltage to specific underlying intramural structures within the 3D volume of the myocardial wall, have insufficient resolution, and are restricted to surface measurements. In addition, optical recordings contain artifacts, such as artificially-created boundary conditions [9], [10] and distortion due to photon scattering [11]. Nonetheless, indirect experimental approaches have provided important insights into the interaction of fine-scale tissue structures and external electric fields. Microscopically, myocyte monolayer studies have demonstrated VEs induced around inexcitable clefts [12]. Macroscopically, optical mapping of isolated left ventricle (LV) wall wedge preparations has demonstrated shock-induced isolated regions of positive and negative polarisations within the bulk of the wall, distant from the surfaces [9], [13]. Thus, given the difficulties of optical mapping, computational models may be beneficial.

Blood vessels represent the largest discontinuities within the myocardial wall, occupying a significant volume, and thus presenting an important, yet hereto uninvestigated, substrate for VEs. Recent advances in magnetic resonance (MR) imaging [14] have facilitated the inclusion of unprecedented levels of anatomical detail, including representations of the coronary vascular system within whole ventricular computational models [15], [16]. However, recent histological analysis [14], [17] has highlighted two important features, yet to be incorporated into such models: (1) a relatively thick vessel lumen wall bounded by connective tissue, through which the passage of current has yet to be experimentally characterised, and (2) that myofibres negotiate around vessels and do not originate/terminate at them. Such changes in fibre orientation affect VE formation, and therefore represent important modelling considerations. Furthermore, the level of detail by which fibre architecture around vessels needs to be represented within models is also not known, as neither rule-based methods for fibre vector assignment [18], nor diffusion tensor MR [14] can provide high levels of detail around intramural structures.

In this study, we aim to: (1) assess the essential methodological modelling aspects necessary to faithfully incorporate a highly-detailed, experimentally-based representation of blood vessels within a high resolution MR-derived computational finite element model; and, (2) quantify the shock-tissue interaction due to the presence of vessels, and the specific microstructural tissue architecture surrounding them, during external electric field stimulation. We hypothesise that large discontinuities represented by vessel cavities provide an important substrate for secondary source formation, and that fine-scale structure around vessels will significantly influence the magnitude of the witnessed effects.

To achieve our objectives, direct experimental measurements of vessel lumen wall conductivity are performed to parameterise the finite element model. A novel rule-based method for assigning histologically-realistic micro-structural fibre architecture around intramural obstacles is presented. Bidomain simulations are performed to quantify the transmembrane potential response to externally-applied electric shocks of varying strength, and dissect the mechanisms by which the spatial distribution of polarisation relates to underlying histoanatomical tissue architecture. The specific role played by the vessels is analysed through comparison with a simplified equivalent model lacking any intramural structures.

II. Methods

A. Experimental Measurement of Vessel Wall Conductivity

1) Experimental Set-Up—Long, unbranched segments of left-coronary artery and right anterior descending artery were dissected from excised hearts of young New Zealand white rabbits. Excess fatty and connective tissue was carefully removed, and the vessel segments cannulated with a U-shaped, 30 gauge wire electrode. Vessel segments were lowered into a bath of saline solution, such that the base of the vessel segment was submerged. A 20 kHz sinuosoidal voltage, with peak-to-peak amplitude of 5–10 V, was applied between the electrode and bath. The open ends of the vessel segment were kept above the surface of the bath and plugged with silicon, ensuring that all current passed through the vessel walls. The current was recorded for varying voltage levels and used to calculate the resistance of the sample for different submersion depths.

2) Calculation of Conductivity—For a length of cylindrical vessel submerged (s), the conductivity of the sample (σ) can be derived from the following expression

$$\sigma = \frac{l}{\pi d s R} \quad (1)$$

where R is the measured resistance, l the thickness of the vessel wall (the direction through which current passes) and d the vessel diameter. Conductivity values were calculated for different submersion depths (between 40% – 90% total segment length) for each vessel segment. l was derived from d using a wall thickness-to-cavity diameter ratio of 0.036 [19]. Mean conductivity across the vessel wall, averaged over all samples ($n = 8$) was 0.010 ± 0.003 S/m.

B. Computational Model Generation

1) Geometrical Model Construction—A finite element model of an LV wedge preparation was generated directly from a previously published high resolution rabbit MR data set (voxel resolution ≈ 25 μm isotropic) [15], The full resolution grey-scale MR data was first segmented [15] to create a binary (0, 1) voxel image stack, discriminating between tissue and non-tissue. The segmented data set was cropped to produce an LV wedge (Fig.

1(a)) and papillary muscles manually removed, in-line with experimental wedge preparation procedures [13]. Blood vessel cavities within the wedge were identified using a connected component algorithm applied to the segmented image stack, through manual selection of seed points at the top of main vessel trees. Referral back to the MR data set allowed the delineated branches to be identified as arteries or veins. Corresponding numerical tags were then applied to the connected voxel components representing the artery/vein cavities to distinguish them from myocardial tissue or other background material.

The mesh generation software Tarantula (www.meshing.at), which is based upon a previously published algorithm [20], was used to generate a tetrahedral finite element mesh directly from the segmented (and tagged) voxel image stack. The total mesh produced (consisting of myocardial tissue, plus surrounding bath volume) consisted of 2141926 nodes defining 12629186 tetrahedral elements with a mean edge length of 63.3 μm (standard deviation 14.0 μm). Fig. 1(c) shows the vessel tree structures contained within the mesh (arteries shown red, veins blue). Vessel structures identified in the model ranged from approximately 50–500μm in diameter.

2) Functional Representation of Blood Vessel Wall—To represent the reduced electrical conduction through the connective tissue of the vessel lumen wall, elements within the extracellular bath which directly bordered the blood vessel/myocardium interface were tagged and subsequently assigned distinct electrical properties. Fig. 1(d) shows discretisation and property assignment of elements around a vessel.

C. Microscopic Representation of Cardiac Fibre Architecture

Cardiac fibres run primarily in a circumferential (or latitudinal) direction through the LV myocardial wall (i.e., approximately within the *xy*-plane of Fig. 1(b)) with an additional inclination in the apex-base (or longitudinal) direction [18], [21]. The inclination (or helix) angle, α, varies transmurally by approximately 120 degrees from epi- to endocardium, being approximately zero in the mid-wall [18], [21]. Furthermore, and of key relevance to this study, fibres negotiate around intramural structures in a continuous manner [17]. Here, we use a method which successfully represents both of these fundamental aspects of fibre architecture in our model.

1) Laplace-Dirichlet Method—An adapted version of the Laplace-Dirichlet method was implemented to assign cardiac fibre architecture. The method involves computing the solution of an electric potential, Φ, within the tissue between two electrodes using Laplace's equation ($\nabla^2\Phi = 0$) where isotropic conductivity is assumed. A voltage is assigned between the electrodes and no flux conditions are imposed on all other surfaces. Field lines will terminate only on the electrodes and be tangential to all other surfaces. The resulting potential gradient will be smooth and globally point from one electrode to the other, but importantly, navigate around local discontinuities, i.e., holes in the tissue. By solving for two electrode configurations which are orthogonal to each another, a basis set can be constructed which describes the transmural, apicobasal and circumferential fibre components.

2) Application of the Laplace-Dirichlet Method to the Wedge Model—The Laplace-Dirichlet method was used with electrode configurations placed (1) at the two cut vertical transmural faces of the wedge to produce a circumferential electric field (Fig. 2(a), left); and, (2) at the two horizontal cut faces of the wedge, to produce a field in an apex-base direction (Fig. 2(b), left). Computation of the gradient of the potential at each element thus gave, in Fig. 2(a) the local circumferential direction, which can be thought of as the "default" fibre vector direction in the absence of a transmural helix angle, termed $\mathbf{f}_c$, and in

Fig. 2(b) the local apex-base vector direction, termed $\mathbf{f}_a$. The inset panels of Fig. 2(a) & (b) (right) show how in each case the gradient vectors successfully negotiate the intramural structures, as required.

In order to incline the default circumferential vector by α to give the real fibre vector **f**, a linear combination of the unit vectors $\hat{\mathbf{f}}_c$ and $\hat{\mathbf{f}}_a$ was formed

$$\mathbf{f}=\widehat{\mathbf{f}}_c+\gamma\widehat{\mathbf{f}}_a, \quad (2)$$

where γ is a scaling factor whose value depends on α (i.e. $\gamma = \tan\alpha$). For example, for $\hat{\mathbf{f}}_c$ and $\hat{\mathbf{f}}_a$ being perpendicular to one another, as is the case in the bulk of the myocardium away from intramural structural discontinuities, and the required $\alpha = \pi/4$, gives a value of $\gamma = 1$. **f** is then re-normalised to a unit vector. This method has the distinct advantage that the local circumferential and apex-base direction, defined by the gradient vectors of the two Laplace solves, both successfully negotiate around the intramural cavities within the mesh, i.e., they are always tangential to the cavity wall. Thus, forming a linear combination of the two vectors ensures the resulting vectors never penetrate into any intramural cavity.

The functional form of the transmural variation of α through the myocardial wall, used to calculate β in Eq. (2), was derived according to the cubic law proposed by [18], $\alpha=\frac{\pi}{3}(1-2e)^3$, where e is the normalised transmural distance through the myocardial wall, itself given by $e=\frac{d_{endo}}{d_{epi}+d_{endo}}$, with d_{endo} and d_{epi} being the minimum respective distances endocardial and epicardial walls.

Fig. 3 shows a representation of the final fibre vectors within the computational model in a transmural slice along the *xy*-plane, with the colour-bar representing the out-of-plane component of the fibre vectors. As can be seen, the above rule-based method successfully accounts for the transmural variation in helix angle, seen by the change in vector colour from epicardium to endocardium, as well as the continuous fibre structure around intramural cavities, clearly shown in the highlighted region in Fig. 3, right.

D. Modelling Electrical Activation

1) Governing Equations—Electrical activation throughout the ventricular model was simulated using the bidomain equations [6]

$$\nabla\cdot\widehat{\sigma}_i\nabla\phi_i=\beta I_m \quad (3)$$

$$\nabla\cdot\widehat{\sigma}_e\nabla\phi_e=-\beta I_m-I_e \quad (4)$$

$$I_m=C_m\frac{\partial V_m}{\partial t}+I_{ion}(V_m,\eta)-I_s, \quad (5)$$

where ϕ_i and ϕ_e are the intracellular and extracellular potentials, respectively, $V_m = \phi_i - \phi_e$ is the transmembrane voltage, $\widehat{\sigma}_i$ and $\widehat{\sigma}_e$ are the intracellular and extracellular conductivity tensors, respectively, β is the membrane surface to volume ratio, I_m is the transmembrane current density, I_e is an extracellular stimuli, I_S is a transmembrane stimulus,

C_m is the membrane capacitance per unit area, and I_{ion} is the membrane ionic current density which depends on V_m and a set of state variables. At tissue boundaries, no flux boundary conditions are imposed for ϕ_i with ϕ_e being continuous. The tissue is surrounded by a conductive bath with no flux boundary conditions for ϕ_e.

Conductivities were set as in [15]. The vessel lumen wall (g_e^{lum}) was assigned the experimentally-derived value of conductivity found in Section II-A of 0.010 S/m (isotropic) in the extracellular domain. Conductivity of the surrounding extracellular bath (including bath within vessel cavities) was set to 1.0 S/m (isotropic), representing a perfused tissue arrangement. Cell membrane dynamics within the myocardial tissue were represented by a recent rabbit ventricular cell model [22]. To reproduce the asymmetry of the membrane response to strong shocks delivered during the plateau phase of the action potential, the cell model was further augmented [23] with two additional currents, an electroporation current and a hypothetical potassium current that activates at larger positive polarizations beyond +160mV.

2) Computational Considerations—The bidomain equations were solved with the Cardiac Arrhythmia Research Package (CARP) [24]. The specifics of the numerical regimes used in CARP have been described extensively elsewhere [14], [24]. Simulations were performed on the Oxford Supercomputing Centre clusters. Visualisation of results was performed with the custom written Meshalyzer software.

E. Simulation Protocols and Analysis

1) Stimulation Protocol—A transmembrane current pulse of 5×10^{-3} μA/cm^3 was delivered over 1 ms duration via a pacing electrode (Fig. 4) to elicit propagation in a circumferential direction. 100 ms later (ensuring all tissue being refractory), a 5 ms long monophasic shock of varying shock strength (SS) was applied via the electrode configuration (anode/ground) (Fig. 4) to the extracellular bath. The specific corner-shape electrode set-up, with the electrode closest to the epicardium (by default the anode) having an edge-length of 8 mm, compared to 0.6 mm for the endocardial electrode (ground), produced an approximate transmural field, in-line with experimental configurations [9]. Shocks of 1, 4, 10, −10, and 20 V were used, resulting in corresponding field strengths of ≈ 2, 8, 20, −20 and 40 V/cm, as the width of myocardial wall is approximately 0.5 cm throughout.

2) Comparison with Simplified Model—To facilitate direct dissection of the role played by intramural structures, a simplified model was also produced in which all intramural cavities (blood vessels, extracellular cleft spaces) were filled-in at the segmentation stage, prior to meshing. The simplified model contained only myocardial tissue throughout, and had fibre architecture assigned using the same rule-based approach described in Section II-C above. Identical stimulation protocols were applied to both complex and simplified models throughout via similarly placed electrodes.

3) Comparison with Discontinuous Fibre Architecture—To assess the importance of the continuous negotiation of cardiac fibres around intramural cavities, an additional version of the complex model was produced containing a discontinuous fibre field. To achieve this, fibre vectors were mapped-over directly from the simplified model using a nearest neighbour approach on element centroids. Fig. 4(b) shows this discontinuous fibre structure in the same highlighted area as Fig. 3. Unless otherwise stated, the fully continuous representation of fibre architecture within the model (described in Section II-C and shown in Fig. 3) was used.

4) Data Analysis—Shock-end V_m levels and distributions were compared for different SSs between the two models described above. Changes in V_m levels induced by the shock, δV_m (defined as $\delta V_m = V_m^{shock-end} - V_m^{shock-onset}$), were examined throughout *intramural* and *epicardial* regions of the models. The intramural region is defined to contain all nodes in the finite element model which have normalised transmural distances of $0.25 < e < 0.75$, tissue sufficiently distant from external surfaces to be considered unaffected by the direct action of the shock [9], [10]. The epicardial region is defined to contain nodes only residing on the epicardial surface, a common recording site in optical mapping measurements of shock-end VE polarisations. In both cases, points within ±1 mm of the cut transmural surfaces were not included in the analysis to eliminate edge effects.

III. Results

A. Localised Effects of Vessels in Shock Application

1) Qualitative Effects of the Shock—Fig. 5 shows shock-end V_m distributions within both complex and simple models followings shocks of SS 1, 4, 10, −10 and 20 V. For weak shocks (1 V), both models show very little effect of the stimulus, with the vast majority of tissue remaining at the pre-shock polarisation state (~ −10 mV, yellow in colour-scheme). The exception to this is the appearance of small light-blue regions on endocardial surfaces, corresponding to a slight hyperpolarising effect of the shock in these areas.

At intermediate shocks (4 V), the effect of the external stimulus now causes significant depolarisation of tissue on the epicardial surface and hypolarisation on the endocardial surface to a similar extent in both models. However, tissue within the mid-myocardial wall remains largely unaffected in both cases. Furthermore, a heterogeneous distribution of polarisation levels occurs within the tissue at the two points of insertion of a trabeculation (briefly detached from the endocardial surface) labelled in Fig. 5 (SS 4 V, simple model). Where the trabeculation becomes fully detached from the surface, the tube-like structure is seen to form small VEs, with the anodal side depolarised and the cathodal side hyperpolarised.

Fig. 5 also shows that for strong shocks (SS 10,20 V) the stimulus causes significant depolarisation/hyperpolarisation of epicardial/endocardial surfaces, respectively, in both models, increasing with SS. However, strong shocks produce significant mid-myocardial effects in the complex model not present in the simplified model, through the formation of VEs surrounding intramural structures, which become more pronounced at higher strengths. Finally, reversing shock polarity results in a reversal of the effects witnessed above: the endocardium becomes depolarised, the epicardium hyperpolarised, and all of the small-scale VEs (on the trabeculation and surrounding intramural structures) also switch polarity (Fig. 5).

2) Quantitative Effects of the Shock—Transmural V_m profiles were constructed along the dashed-line A shown in Fig. 6(a) for the complex (Fig. 6(b)) and simplified (Fig. 6(c)) model for different SS. In addition, Fig. 6(d) shows the variation of maximum δV_m induced within myocardial tissue immediately adjacent to the cavity (on the ground side) of 3 different sized vessels (each approximately the same distance from the epicardium), with SS. In-line with Fig. 5, Fig. 6(b) and (c) show that as SS increases, both models predict progressively stronger hyperpolarisation levels on the endocardium (up to ≈ −200 mV for SS20), with more strongly depolarised V_m on the epicardium (up to ≈ 100 mV for SS20). Between the endocardium and mid-wall, both models predict very similar transmural V_m profiles, due to the distinct absence of intramural structures along the first part of line A (seen in Fig. 6(a)), and so the two models are both geometrically the same here, with similar

fibre orientations. In both cases, tissue appears to be significantly activated by the shock up until $e \approx 0.25$, corresponding to 0.98 mm from the endocardial tissue-bath interface. Such an observation agrees with theoretical predictions for the fall-off in activated tissue after a few electrotonic space constants (0.3 – 0.5 mm [5]).

However, Fig. 6(a) shows that line A encounters two large sub-epicardial blood vessels ($e \approx$ 0.85-1.0), and runs close to a further two smaller vessels ($e \approx$ 0.4-0.6). Consequently, multiple inflections are seen in the complex model V_m profile in Fig. 6(b) in these regions, the magnitude of which increase with SS, with the simplified profile continuing to vary smoothly (Fig. 6(c)). These sudden inflections arise due to regions of strong positive/ negative polarisation induced towards the cavity edges of the vessels (as seen in Fig. 5). As seen in the plots, the magnitude of V_m on either side of the vessel cavity can reach over ±70 mV in regions where polarisation levels predicted by the smoothly-varying simplified model profile remain ~ 0 mV (e.g. at $e \approx 0.8$). Furthermore, the increase in the magnitude of inflections in V_m across a vessel cavity with SS is underscored by Fig. 6(d) which further shows that the maximum V_m induced around a vessel also increases with vessel diameter. For example, for SS20, maximum δV_m on a large vessel (640μm diameter) is 71.6 mV, compared to 44.9 mV and 9.5 mV for a medium (440μm) and small (210μm) vessel, respectively. Finally, for stronger shocks (SS 10, 20 V/cm), Fig. 6(b) shows that large sub-epicardial vessels attenuate polarisation levels experienced on the epicardial surface in the complex, compared to the simplified model.

B. Implications of the Presence of Vessels in Bulk Myocardium

Here, we quantify how the introduction of secondary sources by vessel structures following shocks affects overall polarisation levels of the bulk-myocardium. Fig. 7 (left) quantifies the percentage of nodes in the intramural region with δV_m negatively affected (< −10 mV, blue), relatively unaffected (between −10 and 10 mV, green), and positively affected (> 10 mV, yellow) by the shock for all positive SS for the complex (left) and simple (right) models. For weak (1 V) and intermediate (4 V) shocks, almost the entire intramural regions in both models are relatively unaffected by the shock: 100% and 98.9 % of the intramural region have $-10 < \delta V_m < 10$ for SS of 1 V and 4 V, respectively, for the complex model and 100% and 100% for the simplified model. However, for stronger shocks, these values become significantly reduced in the complex model as a larger proportion of intramural nodes are directly activated by the shock due to the widespread presence of secondary sources: for SS of 10 V, 88.6% of the intramural region have $-10 < \delta V_m < 10$, which is further reduced to just 67.1% for a SS of 20 V. In contrast, the absence of secondary sources in the simplified model leads to this percentage remaining consistently high at 98.7% and 89.7% for 10 V and 20 V shocks, respectively.

Fig. 7 (right) quantifies the percentage of nodes in the epicardial region with δV_m levels < 50 mV (blue), between 50 and 150 mV (green), and > 150 mV (yellow). As observed in Fig. 5, for weak shocks (1 V) the entire tissue, including epicardial the surface, is relatively unaffected by the shock in both models: 100% of epicardial nodes have $\delta V_m < 50$ V in the complex model, which is matched in the simplified model (100%). As SS increases, the percentage of nodes with stronger polarisation levels increases in both models. However, the combination of a large number of large sub-epicardial vessels in the complex model, along with the formation of VEs around these vessels for stronger shocks (with the hyperpolarised tissue on the anodal, or epicardial, side of the cavity) as seen in Fig. 5, means that for intermediate and strong shocks, epicardial tissue within the simple model consistently experiences stronger polarisation levels than the complex model. For example, for SS 4 V the simple model has just 24.9% nodes with $\delta V_m < 50$ V, compared to 32.9% for the complex model. In addition, for SS of 20 V, the percentage of the epicardial region

experiencing in $\delta V_m > 150$ mV the simple model is 76.6%, compared to just 60.9% in the complex model.

C. Role of Connective Tissue Lumen Wall in Far-Field Affects

To investigate the specific effect of the change in extracellular conductivity across the vessel wall measured in Section II-A on the surrounding tissue, the above protocols were repeated, varying the value of g_e^{lum}. Firstly, the effect of not modelling the presence of the lumen wall at all was examined. Fig. 8(a) (left) shows the shock-end V_m distribution for SS of 20 V (to provide an upper limit on the effects seen) for $g_e^{lum}=1.0$ S/m, i.e. equal to the conductivity of the surrounding bath within the cavity, termed the *normal* case. Here, the specific distribution of V_m within the tissue appears similar to that seen in Fig. 5 (SS 20 V, complex model) where $g_e^{lum}=0.010$ S/m (the experimentally-obtained value). However, important differences do exist which are quantified in Fig. 8(a) (right) showing a difference map of the magnitude of the shock-end V_m distribution in the normal case, relative to the experimentally-derived case i.e. V_m distribution of Fig. 8(a) (left) minus that of Fig. 5 (SS 20 V, complex model). The difference map demonstrates that the majority of the tissue shows almost no difference at all between the two protocols (green in colour-scale). However, significant differences localised around vessel cavities (shown by the highlighted region) are present, generally with magnitudes of < ±50 mV, although max/min differences within the entire domain were 110.6/ − 121.7 mV. Comparing left and right panels of Fig. 8(a) we note that the insulating effect of the lumen wall acts to modulate the magnitude of secondary sources around the vessels: not representing the lumen reduces the extent of the intramural region experiencing changes in polarisation levels of $-10\text{mV} < \delta V_m < 10\text{mV}$ from 67.1% (Fig. 7) to 57.7%, and reduces the percentage of epicardial nodes experiencing $\delta V_m > 150$mV from 60.9% to 46.6%.

Secondly, potential variability in the experimentally-derived vessel lumen wall conductivity was investigated. Fig. 8(b) quantifies the effect of such changes in g_e^{lum}, showing difference maps of the magnitude of the shock-end V_m distribution for differing values of g_e^{lum}, relative to the actual experimentally-derived case ($g_e^{lum}=0.010$ S/m). As witnessed, reducing g_e^{lum} by factors of 100 (left) and 10 (centre) produces relatively small changes in the difference map (max/min differences were 9.4/ − 11.5 mV and 8.5/ − 10.1 mV, respectively), whereas increasing g_e^{lum} by a factor of 10 (right) produces a more significant change (max/min differences were 51.1/ − 45.8 mV. Note that increasing g_e^{lum} by 100 was not examined, as this is close to the normal case value of g_e^{lum} examined in Fig. 8(a).

D. Role of Microscopic Fibre Structure in Far-Field Affects

To evaluate the importance of the continuous negotiation of cardiac fibres around intramural structures, the protocol was repeated using the discontinuous representation of fibre architecture. Fig. 9(a) shows the shock-end V_m distribution within the complex model, incorporating the discontinuous fibre structure, for SS 20 V. A highlighted area, showing the formation of a far-field VE around a major blood vessel, is shown (bottom, left); for comparison, the same highlighted region from Fig. 5 (SS 20 V) is also shown (bottom, right). Evident in these highlighted regions is that a discontinuous fibre structure within the model significantly accentuates the formation of VEs around vessel cavities, increasing the spatial extent of tissue experiencing hyperpolarisation/depolarisation in the neighbourhood of the vessel, relative to the continuous case. Such qualitative observations are quantified in Fig. 9(b), showing a difference map of the shock-end V_m levels within the discontinuous relative to the continuous fibre model. Here, differences are largely confined to the vicinity of intramural cavities, in many places reaching levels of over +50/ −50 mV. Regions away

from such structures, however, are seen to have a difference close to 0 mV. The max/min difference throughout the model is 108.4/ − 150.3 mV.

Furthermore, the percentage of nodes within the intramural region experiencing changes in polarisation levels of $-10\text{mV} < \delta V_m < 10\text{mV}$ decreases from 67.1% (shown in Fig. 7) to 63.7% using the discontinuous representation, thus showing that the latter approach overestimates the volume of intramural tissue activated by the shock relative to the continuous case. Furtherfore, for vessels close to the epicardial surface, the increase in the spatial extent of hyperpolarised tissue on the anodal side of the vessel is seen to further modulate the magnitude of the strong positively-induced polarisation close to the epicardial surface in that region, demonstrated by the two highlighted regions in Fig. 9(b) (bottom). This in turn leads to a reduction of the percentage of epicardial nodes experiencing $\delta V_m <$ 150mV, being reduced from 60.9% in the continuous case to 51.7% in the discontinuous case.

IV. Discussion

Large-scale intramural discontinuities, such as blood vessels, have been suggested to provide an important substrate in the formation of intramural VEs, facilitating activation of the bulk myocardium and hence successful defibrillation [5], [9], [12]. However, direct experimental evidence of the mechanistic role played by such structures is lacking, due to the challenges of faithfully recording the effect of intramural discontinuities of different spatial scales, and relating the measurements to underlying 3D myocardial structure. This present study sought to address these issues by incorporating a histo-anatomically based representation of coronary blood vessels within a computational LV wedge model to perform quantitative investigation into the shock-tissue interaction in the presence of vessels during external field stimulation.

Blood Vessels and Secondary Source Formation During Shocks

Previous experimental optical mapping studies have highlighted the existence of positive and negative regions of polarisation within the intramural wall during shock application in LV wedge preparations [9], [13], [25]. However, due to the 2D nature of surface recordings, combined with limitations in optical resolution and inherent distortions present in the mapping technique, associating the VEs recorded with specific underlying anatomical features within the sample has so far not been possible. Here, we have demonstrated that shock-induced VEs form around discontinuities represented by intramural blood vessels, as well as large extracellular cleft spaces also present in the model (as witnessed in Fig. 5). The magnitude and distribution of these secondary sources was seen to increase with shock strength, and reversed sign upon reversal of shock polarity, in accordance with experimental findings [9]. Furthermore, the existence of intramural VEs have been indirectly characterised experimentally by the existence of sharp inflections in the shock-end δV_m profile transmurally across the wall [9], [12] and by an increase in the intramural mapped tissue area directly activated by the shock with SS [9]. The findings from this study, chiefly in Fig. 6 and Fig. 7, qualitatively agree with these previous experimental observations [9], [12], as well as computational studies using geometrically simplistic LV wedge representations [10].

Finally, the formation of intramural VEs (both qualitatively in Fig. 5 and quantitatively in Fig. 6 and 7) became only significantly apparent between SS of 8–20 V/cm. Although not precisely identified here, this SS range also correlates closely with the lower SS limit required to successfully defibrillate real tissue [26], and thus the role of intramural discontinuities such as vessels could provide an explanation for the effectiveness of clinically-used defibrillation shocks of 6–10 V/cm.

Implications for Epicardial V_m Recordings

Our results show that the locality of large coronary vessels with the epicardial surface significantly attenuates the shock-induced polarisation experienced by the epicardium due to the formation of VEs around the vessel perimeter. During anodal shocks, the epicardial surface of the ventricular wall is strongly depolarised. However, as VEs form around the vessels, proximal tissue on the epicardial side of the vessel becomes hyperpolarised, whilst tissue on the endocardial side is depolarised. In the case of sub-epicardial vessels, the close proximity of these virtual cathodes on the epicardial side of the vessel with the strongly depolarised epicardial surface acts to modulate the polarisation experienced by tissue on the epicardium itself. Due to the large number of vessels close to the epicardium, such an effect was seen to reduce the polarisation of the epicardium as a whole (Fig. 7), as well as occurring as a localised effect around a specific vessel (Fig. 6).

Knowledge of how sub-epicardial vessels affect surface recordings of V_m during shocks could have important implications in the interpretation of epicardial optical mapping recordings [25]. Specifically, it could help to explain previous discrepancies in the quantitative comparison between optical recordings and computational simulations using more simplified models lacking intramural structures [11]. Previous simulation studies have successfully demonstrated how the distortive averaging effect, resulting from photon scattering inherent to the optical mapping technique, acts to modulate the apparent optically-recorded epicardial shock-end VE polarisation [11]. Nonetheless, there still exists a disparity between simulation and experiment, with simplified models still over-estimating the magnitude of the shock-induced epicardial response. Considering the evidence presented in this study, we believe that the inclusion of intramural structures could account for such quantitative differences in shock-end measurements, which thus represents an important consideration in future combined studies and experimentally-driven analysis of tissue-shock interaction during defibrillation.

Role of Histo-Anatomical Microstructure Around Vessels

As computational cardiac models include ever-increasing levels of histo-anatomical detail [7], [14], [15], [16], fueled by advances in cardiac imaging techniques and our computational abilities, it is becoming increasingly important to correctly parameterise these models in order to faithfully represent the function of these additional structural features. For example, although some of the most recent cardiac models have contained representations of blood vessel structures [7], [15], [16], [27], none have included the effects, in a model parameter sense, of the insulating effects of the vessel lumen wall, known from histological analysis to contain thick layers of connective tissue [14], [17]. For the first time, we have experimentally measured the conductivity of the vessel lumen wall of rabbit coronary arteries (measured value 0.010 S/m), and used this to parameterise the vessel cavity/ myocardium interface within our computational LV wedge model.

Our results have demonstrated that the faithful representation of the vessel lumen wall is an important parameter to include within anatomically complex models when examining the effects of external shocks on blood vessels. We have shown that the insulating effects of the lumen wall act to attenuate the formation of VEs within the myocardium. We believe that, due to the reduced conductivity within the wall (represented by g_e^{lum}), it becomes less preferential for current within the tissue to traverse the discontinuity (represented by the vessel) by passing through the lumen wall into the cavity and back on the other side. Thus, more of the shock-induced current remains within the tissue domain, athough redistribution between intra-/extracellular spaces also occurs. In the case where no lumen is represented within the model, this low resistance pathway (directly through the cavity) encourages redistribution of current between domains, as the conductivity of the bath is significantly

higher (1.0 S/m) than either the intra-/extracellular conductivity of the tissue, accentuating the formation of VEs (Fig. 8(a)). Furthermore, our parameter sensitivity analysis (Fig. 8(b)) showed relatively small changes in over-all VE effects as g_e^{lum} was varied over an order of magnitude of the experimentally derived value, and thus we believe that any small differences in effective g_e^{lum} between arteries and veins will have little influence on the results presented. However, as g_e^{lum} becomes approximately greater than the tissue conductivities, more current passes through into the vessel cavity and VE effects become greater (Fig. 8(a)).

A further anatomical consideration when incorporating vessels into computational cardiac models is the faithful representation of the smooth negotiation of fibres around intramural blood vessels [17]. The novel rule-based method, developed in this study, for incorporating such detailed fibre architecture has allowed its incorporation into our MR-derived wedge model. Our results demonstrate that the magnitude and distribution of VEs induced around vessels following shocks was significantly reduced with accurate negotiation of myofibres, compared to when the structures are ignored and fibres are allowed to begin/terminate at vessel cavities. As fibres negotiate around vessels, the intracellular discontinuity represented by the vessel cavity is reduced. As such, it is preferential for intracellular current to pass around the structure within the smoothly negotiating domain of the myocardial tissue than to cross into the extracellular domain of the cavity and back again (forming a VE). The specific magnitude of this affect will, however, no-doubt depend upon the individual size, shape, location and orientation of the vessel, as well as strength of the applied shock. Our novel method for smooth fibre vector assignment represents, to date, the only means of incorporating such information into large-scale anatomically-realistic computational models. As such it has allowed us to identify the significant importance of accurately representing fibre architecture in the vicinity of blood vessels, and other intramural structures, when investigating shock-tissue interactions.

Study Limitations

Direct quantitative comparison of simulation results to optical mapping recordings is difficult, primarily due to distortive effects of optical mapping [11]. We are currently developing modelling techniques to simulate optical signals from anatomically complex models. Thus, our aim here has been to relate secondary source formation to histo-anatomical structure, to aid interpretation of future experimental investigations. Future validation will involve comparison of post-shock total activation times with previous experimental recordings [13], and in-depth analysis of activation sequences following shock.

Although our MR-derived model contains larger extracellular cleft spaces, it does not contain fine-scale detail regarding intermyolaminar clefts, as seen in histological reconstruction models [7], [27]. This results from higher resolution of histology, combined with pre-processing, which dehydrates tissue, reducing myocyte volume, and exacerbating apparent cleft sizes. While clefts are undoubtedly found throughout the myocardium and have been identified as an important substrate for secondary sources [12], it remains an open question as to what extent the accentuated cleft size affects VE formation.

V. Conclusions

In summary, this study has furthered our understanding of the importance of the coronary vasculature during defibrillation. Through development of a high resolution LV wedge model, containing faithful structural and functional representations of intramural blood vessels, we have shown how the discontinuities caused by vessel structures act as a substrate for the formation of intramural VEs, the magnitude and distribution of which depend

Europe PMC Funders Author Manuscripts

strongly on the specific myofibre orientation around the vessels, as well as the insulating effects of the lumen wall conductivity. Consequently, these regions of strongly polarised tissue facilitate bulk activation of the LV wall, as well as reduction of polarisation recorded from the epicardial surface. These findings have important implications for the future construction of highly detailed cardiac models, the interpretation of optical mapping recordings of tissue shock interactions, and defibrillation mechanisms.

Acknowledgments

The authors thank the teams of Prof. D. Gavaghan, Dr P. Kohl and Dr J. Schneider (University of Oxford) for access to MR data from their 3D Heart Project, and acknowledge the use of resources provided by Oxford Supercomputing Centre.

M. Bishop is supported by the Wellcome Trust through a Sir Henry Wellcome Postdoctoral Fellowship. P. Boyle is supported by NSERC and the Alberta Ingenuity Fund. G. Plank is supported by Austrian Science Fund FWF grant (F3210-N18). D. Welsh is supported by the Natural Science and Engineering Research Council of Canada. E. Vigmond is supported by NSERC and MITACS.

Biographies

Martin J. Bishop received the M. Phys. degree in Physics (’03) and the D. Phil. degree in Computational Biology (’08) from the University of Oxford, UK. He is currently a Sir Henry Wellcome Postdoctoral Fellow based at the Computing Laboratory, University of Oxford, UK. His current research interests include computational cardiac modelling and imaging.

Patrick Boyle (S’07) received the B.Sc. degree in Computer Engineering from the University of Calgary, Calgary, AB, Canada, in 2005. He is currently a Ph.D. candidate in Electrical Engineering with a specialization in Biomedical Engineering at the University of Calgary. Currently, his primary research interest is using biophysical modelling to explore the role of the Purkinje system in the development, maintenance, and termination of lifethreatening cardiac arrhythmias.

Gernot Plank received the M.Sc. (’96) and Ph.D. (’00) degrees in electrical engineering from the Institute of Biomedical Engineering, Technical University of Graz, Austria. Currently he is Associate Professor with the Institute of Biophysics, Medical University of

Graz, Austria and Academic Fellow with the Oxford e-Research Centre, University of Oxford, UK. Prior, he was a Postdoctoral Fellow with the Technical University of Valencia, Spain (’00–’02), the University of Calgary, AB, Canada (’03) and Marie Curie Fellow with Johns Hopkins University (’06–’08). His research interests include computational modeling of cardiac bioelectric activity, microscopic mapping of the cardiac electric field and defibrillation.

Donald Welsh received his PhD in Biophysics from the University of Guelph in 1994. He was a postdoctoral fellow at the John B. Pierce Laboratory (Yale University) (’94–’98) and the University of Vermont from (’98–’01). He is currently an Associate Professor with the Department of Physiology and Pharmacology, University of Calgary, AB, Canada. He is a senior scholar with the Alberta Heritage Foundation for Medical Research and holds a Canada Research Chair. His research centers on vascular biology and the electrical basis of smooth muscle contraction.

Edward Vigmond (S’96 M’97) received his B.A.Sc. (’88) in Electrical and Computer Engineering from the University of Toronto, from which he also received his M.A.Sc. (’91) and Ph.D. (’96) in the Institute of Biomedical Engineering. He was a postdoctoral fellow at the University of Montreal (’97–’99) and Tulane University (’99–’01). Presently, he is an associate professor at the University of Calgary, Department of Electrical and Computer Engineering, and is also the Director for the Centre for Bio-engineering Research and Education. His research interests include numerical field computation, biomedical signal processing, and modeling of nonlinear biosystems.

References

[1]. Zipes D, Fischer J, King R, Nicoll A, Jolly W. Termination of ventricular fibrillation in dogs by depolarizing a critical amount of myocardium. Am J Cardiol. 1975; 36:37–44. [PubMed: 1146696]

[2]. Zhou X, Daubert J, Wolf P, Smith W, Ideker R. Epicardial mapping of ventricular defibrillation with monophasic and biphasic shocks in dogs. Circ Res. 1993; 72:145–160. [PubMed: 8417837]

[3]. Sobie EA, Susil RC, Tung L. A generalized activating function for predicting virtual electrodes in cardiac tissue. Biophys J. 1997; 73:1410–23. [PubMed: 9284308]

[4]. Fishler MG. Syncytial heterogeneity as a mechanism underlying cardiac far-field stimulation during defibrillation-level shocks. J Cardiovasc Electrophysiol. 1998; 9:384–94. [PubMed: 9581954]

[5]. Newton JC, Knisley SB, Zhou X, Pollard AE, Ideker RE. Review of mechanisms by which electrical stimulation alters the transmembrane potential. J Cardiovasc Electrophysiol. 1999; 10:234–43. [PubMed: 10090228]

[6]. Plonsey R, Barr R. Effect of microscopic and macroscopic discontinuities on the response of cardiac tissue to defibrillating (stimulating) currents. Med Biol Eng Comp. 1986; 24:130–136.

[7]. Hooks D, Tomlinson K, Marsden S, LeGrice I, Smaill B, Pullan A, Hunter P. Cardiac microstructure: implications for electrical propagation and defibrillation in the heart. Circ Res. 2002; 91:331–338. [PubMed: 12193466]

[8]. Trayanova N, Skouibine K, Aguel F. The role of cardiac tissue structure in defibrillation. Chaos. 1998; 8:221–233. [PubMed: 12779723]

[9]. Fast VG, Sharifov OF, Cheek ER, Newton JC, Ideker RE. Intramural virtual electrodes during defibrillation shocks in left ventricular wall assessed by optical mapping of membrane potential. Circulation. 2002; 106:1007–14. [PubMed: 12186808]

[10]. Plank G, Prassl A, Hofer E, Trayanova NA. Evaluating intramural virtual electrodes in the myocardial wedge preparation: simulations of experimental conditions. Biophys J. 2008; 94:1904–15. [PubMed: 17993491]

[11]. Bishop MJ, Rodriguez B, Qu F, Efimov IR, Gavaghan DJ, Trayanova NA. The role of photon scattering in optical signal distortion during arrhythmia and defibrillation. Biophys J. 2007; 93:3714–26. [PubMed: 17978166]

[12]. Fast V, Rohr S, Gillis A, Kleber A. Activation of cardiac tissue by extracellular electrical shocks: Formation of secondary sources at intercellular clefts in monolayers of cultured myocytes. Circ Res. 1998; 82:375–385. [PubMed: 9486666]

[13]. Sharifov OF, Fast VG. Optical mapping of transmural activation induced by electrical shocks in isolated left ventricular wall wedge preparations. J Cardiovasc Electrophysiol. 2003; 14:1215–22. [PubMed: 14678138]

[14]. Plank G, Burton RAB, Hales P, Bishop M, Mansoori T, Bernabeu MO, Garny A, Prassl AJ, Bollensdorff C, Mason F, Mahmood F, Rodriguez B, Grau V, Schneider JE, Gavaghan D, Kohl P. Generation of histo-anatomically representative models of the individual heart: tools and application. Phil Trans Roy Soc A. 2009; 367:2257–92. [PubMed: 19414455]

[15]. Bishop M, Plank G, Burton R, Schneider J, Gavaghan D, Grau V, Kohl P. Development of an anatomically-detailed mri-derived rabbit ventricular model and assessment of its impact on simulation of electrophysiological function. Am J Physiol Heart Circ Physiol. 2010

[16]. Vadakkumpadan F, Rantner LJ, Tice B, Boyle P, Prassl AJ, Vigmond E, Plank G, Trayanova N. Image-based models of cardiac structure with applications in arrhythmia and defibrillation studies. J Electrocardiol. 2009:1–10. [PubMed: 19004454]

[17]. Gibb M, Bishop M, Burton R, Kohl P, Grau V, Plank G, Rodriguez B. The role of blood vessels in rabbit propagation dynamics and cardiac arrhythmias. LNCS. 2009; 5528:268–276.

[18]. Potse M, Dubé B, Richer J, Vinet A, Gulrajani RM. A comparison of monodomain and bidomain reaction-diffusion models for action potential propagation in the human heart. IEEE Trans Biomed Eng. 2006; 53:2425–35. [PubMed: 17153199]

[19]. Tomanek RJ, Palmer PJ, Peiffer GL, Schreiber KL, Eastham CL, Marcus ML. Morphometry of canine coronary arteries, arterioles, and capillaries during hypertension and left ventricular hypertrophy. Circulation Research. 1986; 58:38–46. [PubMed: 2935323]

[20]. Prassl AJ, Kickinger F, Ahammer H, Grau V, Schneider JE, Hofer E, Vigmond EJ, Trayanova NA, Plank G. Automatically generated, anatomically accurate meshes for cardiac electrophysiology problems. IEEE Trans Biomed Eng. 2009; 56:1318–30. [PubMed: 19203877]

[21]. Streeter DD, Spotnitz HM, Patel DP, Ross J, Sonnenblick EH. Fiber orientation in the canine left ventricle during diastole and systole. Circ Res. 1969; 24:339–47. [PubMed: 5766515]

[22]. Mahajan A, Shiferaw Y, Sato D, Baher A. A rabbit ventricular action potential model replicating cardiac dynamics at rapid heart rates. Biophys J. 2008; 94:392–410. [PubMed: 18160660]

[23]. Ashihara T, Trayanova NA. Asymmetry in membrane responses to electric shocks: insights from bidomain simulations. Biophys J. 2004; 87:2271–82. [PubMed: 15454429]

[24]. Vigmond E, Hughes M, Plank G, Leon L. Computational tools for modeling electrical activity in cardiac tissue. J Electrocardiol. 2003; 36:69–74. [PubMed: 14716595]

[25]. Sharifov OF, Fast VG. Intramural virtual electrodes in ventricular wall: effects on epicardial polarizations. Circulation. 2004; 109:2349–56. [PubMed: 15117837]

[26]. Wharton J, Wolf P, Smith W, Chen P, Frazier D, Yabe S, Danieley N, Ideker R. Cardiac potential and potential gradient fields generated by single, combined, and sequential shocks during ventricular defibrillation. Circulation. 1992; 85:1510–1523. [PubMed: 1555291]

[27]. Hooks DA, Trew ML, Caldwell BJ, Sands GB, LeGrice IJ, Smaill BH. Laminar arrangement of ventricular myocytes influences electrical behavior of the heart. Circ Res. 2007; 101:e103–12. [PubMed: 17947797]

Europe PMC Funders Author Manuscripts

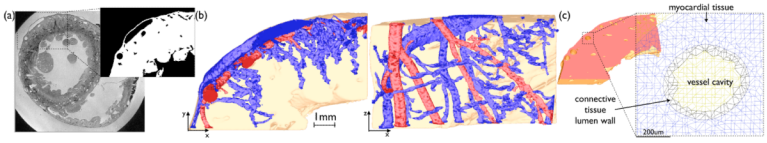

Fig. 1.

Computational model generation. (a) Axial slice through the raw MR rabbit data set, showing the selected region of the LV free wall used to produce the wedge model and the final segmentation of this area with papillary muscles manually removed. (b) Identification of artery (red) and vein (blue) vessel trees within the finite element wedge model. (c) Example of tagged elements within the mesh representing the vessel lumen wall (black) as distinct from the surrounding myocardium (blue) or other extracellular bath region (yellow).

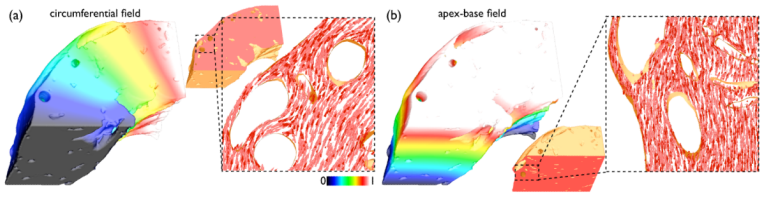

Fig. 2.

Results of Laplace-Dirichlet solves within the wedge model with electrodes placed to produce circumferential (a) and apex-base (b) fields. In each case, vectors representing explicit field gradients are shown in horizontal and vertical slices through the model, respectively.

Europe PMC Funders Author Manuscripts

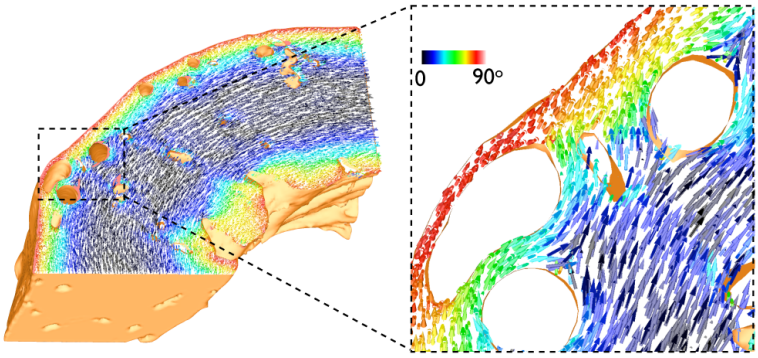

Fig. 3.
Final representation of fibre vectors within the wedge model visualised in a slice along the *xy*-plane. Colour-bar represents the out-of-plane component of the fibre vectors.

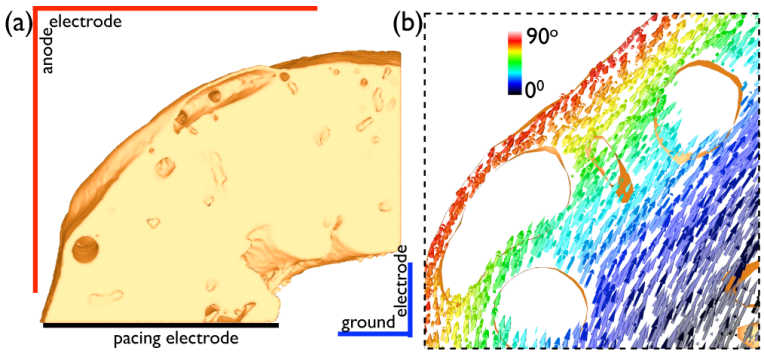

Fig. 4.
(a) Electrode set-up for pacing and delivery of external field stimuli. (b) Discontinuous representation of fibre architecture within the complex model, highlighting the same region shown in Fig. 3(b).

Europe PMC Funders Author Manuscripts

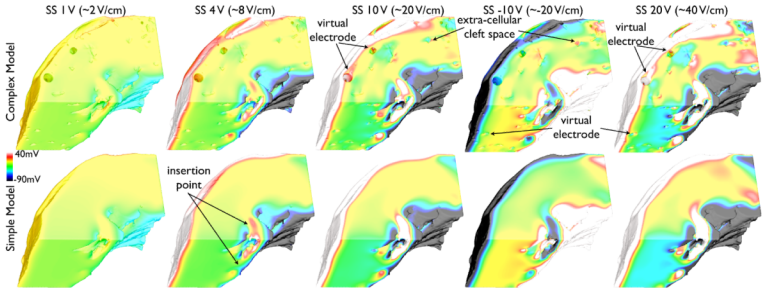

Fig. 5.

Shock-end V_m distributions within the complex (top) and simplified (bottom) models following application of external stimuli of varying SS.

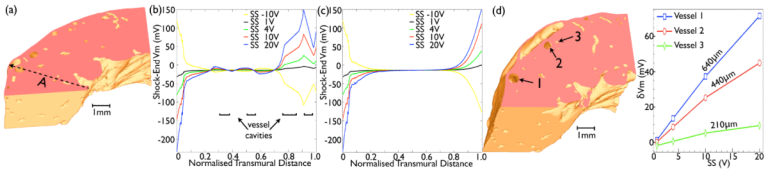

Fig. 6.

Quantitative analysis of transmural V_m profile. (a) Bi-sectional cut through complex wedge model along *xy*-planes showing positions of transmural lines for plotting V_m values. (b) & (c) Variation in V_m along transmural line A for SS of −10 V (yellow), 1 V (black), 4 V (green), 10 V (red) and 20 V (blue) in the complex (b) and simple (c) model. (d) Variation in maximum δV_m of tissue (on ground side) adjacent to 3 different diameter vessels with SS.

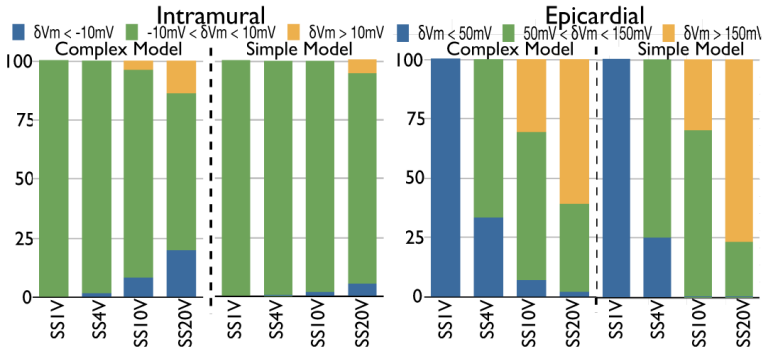

Fig. 7.

Histograms showing the percentage of nodes in the intramural region (left) with δV_m levels < −10 mV (blue), between −10 and 10 mV (green), and > 10 mV (yellow); and, epicardial region (right) with δV_m levels < 50 mV (blue), between 50 and 150 mV (green), and > 150 mV (yellow), for different SS for complex and simple models.

Europe PMC Funders Author Manuscripts

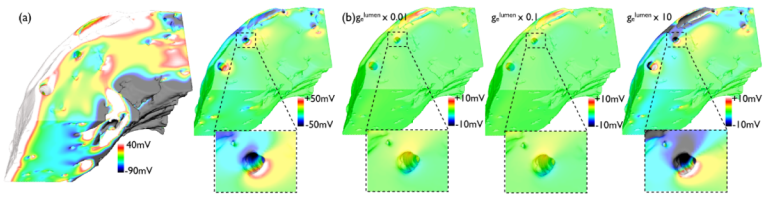

Fig. 8.

(a) (left) Shock-end V_m distribution (SS 20 V) within complex model for the case where the reduced conductivity of the lumen wall (Fig. 1(d)) has not been represented (i.e. g_e^{lum}=1.0 S/m). (right) Difference map of V_m distribution for normal case (g_e^{lum}=1.0 S/m, left panel) minus that of experimentally-derived case (g_e^{lum}=0.010 S/m), with selected region in vicinity of large vessel highlighted. (b) Difference maps of V_m distributions (SS 20 V) for varying g_e^{lum} conductivities minus V_m distribution of experimentally-derived case (Fig. 5), with selected region in vicinity of large vessel highlighted.

Europe PMC Funders Author Manuscripts

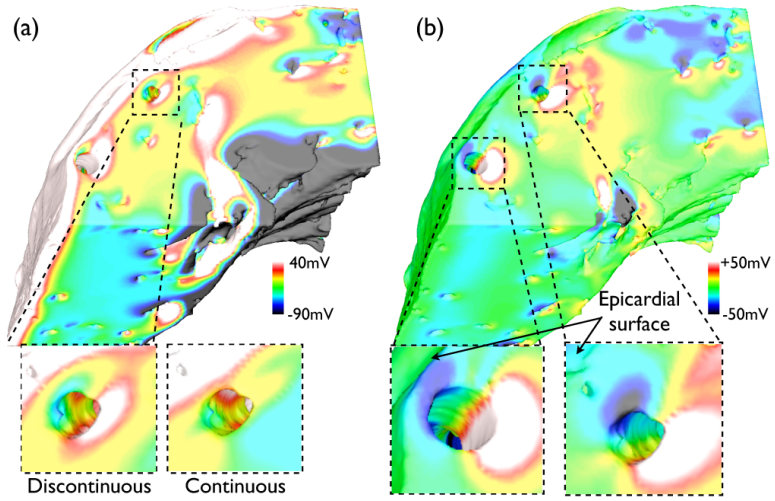

Fig. 9.

(a) Shock-end V_m distribution (SS 20 V) within complex model with discontinuous fibre architecture, with distribution near large blood vessel highlighted (bottom, left) and corresponding V_m distribution with continuous fibre architecture from Fig. 5 (SS 20 V, complex model) (bottom, right). (b) Difference map of V_m distribution of panel (a) minus that of Fig. 5 (SS 20 V, complex model), with selected regions near large vessels highlighted right.

Europe PMC Funders Author Manuscripts